Open Archive Toulouse Archive Ouverte (OATAO)

OATAO is an open access repository that collects the work of Toulouse researchers and makes it freely available over the web where possible.

Any correspondence concerning this service should be sent to the repository administrator: staff-oatao@listes.diff.inp-toulouse.fr

From ceramic–matrix nanocomposites to the synthesis of carbon nanotubes

P. Coquay [a,*], Ch. Laurent [b], A. Peigney [b], O. Quénard [b], E. De Grave [a] and R.E. Vandenberghe [a]

[a] NUMAT, Department of Subatomic and Radiation Physics, University of Gent, Proeftuinstraat 86, B-9000 Gent, Belgium
[b] Laboratoire de Chimie des Matériaux Inorganiques, ESA CNRS 5070, Université Paul-Sabatier, 31062 Toulouse cedex 4, France

The selective reduction in H_2 of oxide solid solutions produces nanocomposite powders in which transition metal nanoparticles are dispersed inside and on the surface of the oxide matrix grains. When using a H_2/CH_4 reducing atmosphere, the metal nanoparticles that form on the surface of the oxide grains act as catalysts for the CH_4 decomposition and, because of their small size at high temperatures ($>800°C$), favor the *in-situ* nucleation and growth of single-wall and thin multiwall carbon nanotubes. This article reviews our results on the synthesis and characterization of M–$MgAl_2O_4$ (M $=$ Fe, Fe/Co, Fe/Ni) nanocomposite powders, without and with carbon nanotubes, emphasizing the information that can be derived from Mössbauer spectroscopy as a complement to other characterization techniques.

Keywords: carbon nanotubes, metal nanoparticles, nanocomposites, Mössbauer spectroscopy

1.   Introduction

The term "nanocomposite" originates from the works of Roy and co-workers in the early eighties [1–3]. It applies to composite systems containing at least one Gibbsian solid phase nanometric in size in at least one dimension, which encompasses all associations between metallic, ceramic and organic materials. Ceramic–matrix nanocomposites have been widely studied in recent years, notably metal–oxide materials which consist of discrete metal nanoparticles dispersed in an oxide matrix (see [4,5] for reviews). Many combinations between the transition and noble metals and oxides such as Al_2O_3, SiO_2, MgO and ZrO_2 have been prepared by a variety of methods, either in the form of powders or thin films [4,5].

One of the present laboratories (Toulouse) has proposed a method based on the selective reduction in H_2 of solid solutions between two or more metallic oxides for the synthesis of nanocomposite powders such as Fe/Cr–Al_2O_3 [6–10], Fe/Ni– and Fe/Ru–Al_2O_3 [11], Fe/Cr–Cr_2O_3 [12], Fe/Co/Ni–MgO [13–15] and Fe/Co/Ni–$MgAl_2O_4$ [16,17]. The size, size distribution and location (inside or at the surface of the oxide

* Author for correspondence: tel.: 0032 (0)9 264 65 69, fax: 0032 (0)9 264 66 97, e-mail: PIERRE. COQUAY@rug.ac.be

grains) of the metal particles depend on several factors related to the materials, including the transition metal content, the mutual solubility of the parent oxides, the specific surface area and the crystalline state of the starting oxide solid solution. Furthermore, the conditions (temperature, duration) of the selective reduction strongly influence the characteristics of the resulting nanocomposite powders.

The initial motivations for these studies were mainly related to the possibility to prepare metal nanoparticles inside the oxide grains. Indeed, it was found that such intragranular particles are protected from oxidation in air up to relatively high temperatures (typically 800°C in alumina-matrix powders) which makes them interesting as model materials for basic research on topics such as magnetism [18,19] or heavy-ion irradiation [20]. Furthermore, the intragranular metal particles are also protected from coalescence during hot-pressing and the presence of intragranular Fe, Cr or Fe/Cr alloy nanoparticles in Al_2O_3 was found to dramatically increase the fracture strength and fracture toughness even for very low metal contents (ca. 1 vol.%) [21].

However, the focus of these studies recently shifted from the intragranular metal particles to those that form on the surface of the oxide grains because it was found that these surface nanoparticles are efficient for the catalytic synthesis of single-wall and thin multiwall carbon nanotubes (CNTs) [22]. CNTs are at the intersection of the science of carbon fibres, which are studied for several decades, and the novel field of fullerenes (Kroto, Smalley and Curl, Nobel Prize for Chemistry 1996). The report by Iijima [23] on the obtaining of carbon tubes with a diameter in the nanometer range and on their relation to the fullerenes triggered a worldwide research effort. A comprehensive description of the structure, properties and applications of CNTs is given in the book by Dresselhaus et al. [24] to which the reader is referred for more details. The synthesis methods of CNTs have been reviewed by Journet and Bernier [25]. Most are based on the sublimation of carbon in an inert atmosphere, such as the electric-arc-discharge process, the laser ablation method and the solar technique, but chemical methods such as the catalytic decomposition of hydrocarbons or carbon monoxide, the electrolysis in a molten ionic salt and the heat-treatment of polymers are also used. Several of these methods involve the use of nanometric metal particles. Laurent et al. [26] have reviewed the various mechanisms proposed for CNTs nucleation and growth from such particles and the micro/nanostructure of the materials obtained by the different methods. In particular, the catalytic decomposition of hydrocarbons on metal particles (Fe, Co, Ni) leads to CNTs when the catalyst particles are sufficiently small (diameter smaller than ca. 6 nm [27,28]). The main difficulty is to obtain these nanometric particles at the relatively high temperature (usually higher than 600°C) required for the formation of CNTs. The reduction of oxide solid solutions [22,28–33] allows to produce metal particles at a high enough temperature for the hydrocarbon gas to somehow interact with them so as to form the CNTs prior to any exaggerate particle growth. In contrast, materials derived from the impregnation of a substrate by a transition metal salt usually consist of large carbon fibres, some of which are hollow, and an even smaller proportion of which indeed are true CNTs (see [34] for a review). This can be overcome only by using a refractory metal such as Mo [35] and Fe/Mo [22,36] or a low metal catalyst loading [37].

This article reviews some of our results on the synthesis and characterization of M–MgAl$_2$O$_4$ (M = Fe, Fe/Co, Fe/Ni) nanocomposite powders [17,33,38], without and with CNTs, emphasizing the information that can be derived from Mössbauer spectroscopy as a complement to other characterization techniques such as scanning and transmission electron microscopy, thermogravimetric analysis and X-ray diffraction. In addition, in the case of the CNTs-containing powders, a method based on chemical analysis and specific surface area measurements [22,29] is used in order to characterize the composites at a macroscopical scale and thus produce data which are more representative of the material than those derived from local techniques.

2. Experimental

2.1. Powder synthesis

Mg$_{1-x}$Fe$_x$Al$_2$O$_4$ (x = 0.05, 0.10, 0.15, 0.20, 0.30, 0.40), Mg$_{0.90}$Fe$_{0.065}$Co$_{0.035}$Al$_2$O$_4$ and Mg$_{0.90}$Fe$_{0.065}$Ni$_{0.035}$Al$_2$O$_4$ solid solutions were prepared by the combustion synthesis route [17,30,31,38,39]. The appropriate amounts of the desired metal nitrates (Mg, Al, Fe, Co, Ni) were mixed in stoichiometric proportions with urea and dissolved in a minimum amount of water in a Pyrex dish, which was then placed in a furnace pre-heated at 600°C. The solution immediately started to boil and undergo dehydration. Within a couple of minutes, a highly exothermic redox reaction occurred, producing the desired oxide as a material swelling to the capacity of the Pyrex dish. The total combustion process was over in less than 5 minutes. The combustion products were either mechanically ground or attrition-milled, the latter process resulting in a finer grain size. Metal–spinel powders were prepared by selective reduction of the oxide solid solutions in flowing H$_2$ at a temperature (noted T_r hereafter) in the range 700–1070°C. For the synthesis of CNTs–metal–spinel composite powders, a H$_2$/CH$_4$ mixture (18 mol.% CH$_4$) was used. The flow rate was fixed at 250 sccm. Heating and cooling rates were equal to 5°C/min.

2.2. Characterization

The powders were studied using scanning and high-resolution transmission electron microscopy (SEM and HRTEM), X-ray diffraction (XRD), thermogravimetric and differential thermogravimetric analysis (TGA and DTG) and ^{57}Fe Mössbauer spectroscopy (MS). The MS spectra were recorded with a ^{57}Co (Rh) source in a conventional time-mode spectrometer with a constant-acceleration drive and a triangular reference signal. Accumulation of the data was performed in 1024 channels until a background of at least 10^6 counts per channel was reached. The spectrometer was calibrated by collecting at room temperature (RT) the spectrum of a standard α-Fe foil and the isomer-shift values quoted hereafter are with reference to this standard. The spectra were generally analyzed assuming symmetrical components with a Lorentzian line shape but strongly asymmetrical Mössbauer patterns were fitted with a hyperfine-field distribution where

each subspectrum is composed of Lorentzian lines. Measurements between 4 K and RT were performed.

The carbon content C_n in the CNTs–metal–oxide powders was determined by flash combustion. Moreover, a method producing results on a macroscopical scale was used for the characterization of the powders. Parts of the composite powders were oxidized in air at 850 or 900°C in order to eliminate all the carbon. The specific surface areas of the powders obtained after reduction (S_r) and of the specimens oxidized at 850 or 900°C (S_o) were measured by the BET method using N_2 adsorption at liquid N_2 temperature. The difference $\Delta S = S_r - S_o$ represents the surface of carbon by gram of composite powder. Since most of the carbon is in the form of nanotubes and since these species have a very high surface area, it has been proposed elsewhere [22] that ΔS essentially represents the quantity of nanotube bundles in the composite powder. The increase in specific surface area by gram of carbon, $\Delta S/C_n$, represents the quality of carbon, a higher figure for $\Delta S/C_n$ denoting more carbon in tubular form and/or a smaller average tube diameter and/or fewer walls [22].

3. Results

3.1. Oxide powders

Analysis of the XRD patterns of the $Mg_{1-x}Fe_xAl_2O_4$ ($0.05 \leqslant x \leqslant 0.40$), $Mg_{0.90}Fe_{0.065}Co_{0.035}Al_2O_4$ and $Mg_{0.90}Fe_{0.065}Ni_{0.035}Al_2O_4$ powders reveals the presence of a spinel phase only. However, the MS spectra present two distributed doublets characteristic of Fe^{2+} and Fe^{3+}. Figure 1(a) shows, for example, the MS spectrum of $Mg_{0.90}Fe_{0.10}Al_2O_4$ measured at 80 K. The presence of Fe^{3+} substituted for Mg^{2+} in the spinel lattice indicates that these oxides are defective spinels, whose formulae can be written as $D_{1-3a}T_{2+2a}()_aO_4$ (D = divalent cation, T = trivalent cation, ( ) = vacancy). Since the spinel lattice has octahedral and tetrahedral sites, the two peaks observed in the distributions of quadrupole splitting for both the Fe^{2+} and Fe^{3+} doublets (figure 1(b) and (c), respectively) could indicate that both cations are distributed among these two sites. However, this is difficult to ascertain due to possible artifacts resulting from the fitting procedure. It is likely that the Fe^{3+} ions are located at or near the surface of the oxide crystallites since they become fully reduced (to the ferrous state) at a temperature as low as 700°C as revealed by the MS analysis. Indeed, this is considerably lower than the temperatures reported for Fe^{3+} ions substituting in the lattices of Al_2O_3 (1300°C), MgO (1200°C) and Cr_2O_3 (1200°C).

3.2. Fe–MgAl₂O₄ powders

The Fe–$MgAl_2O_4$ nanocomposite powders were prepared by reduction in H_2 ($700 \leqslant T_r \leqslant 1000$°C, 1 h) of the $Mg_{1-x}Fe_xAl_2O_4$ oxide solid solutions ($0.05 \leqslant x \leqslant 0.20$). For the sake of briefness, they will be referred to according to the following example: the powder obtained by reduction at 1000°C of the mechanically ground
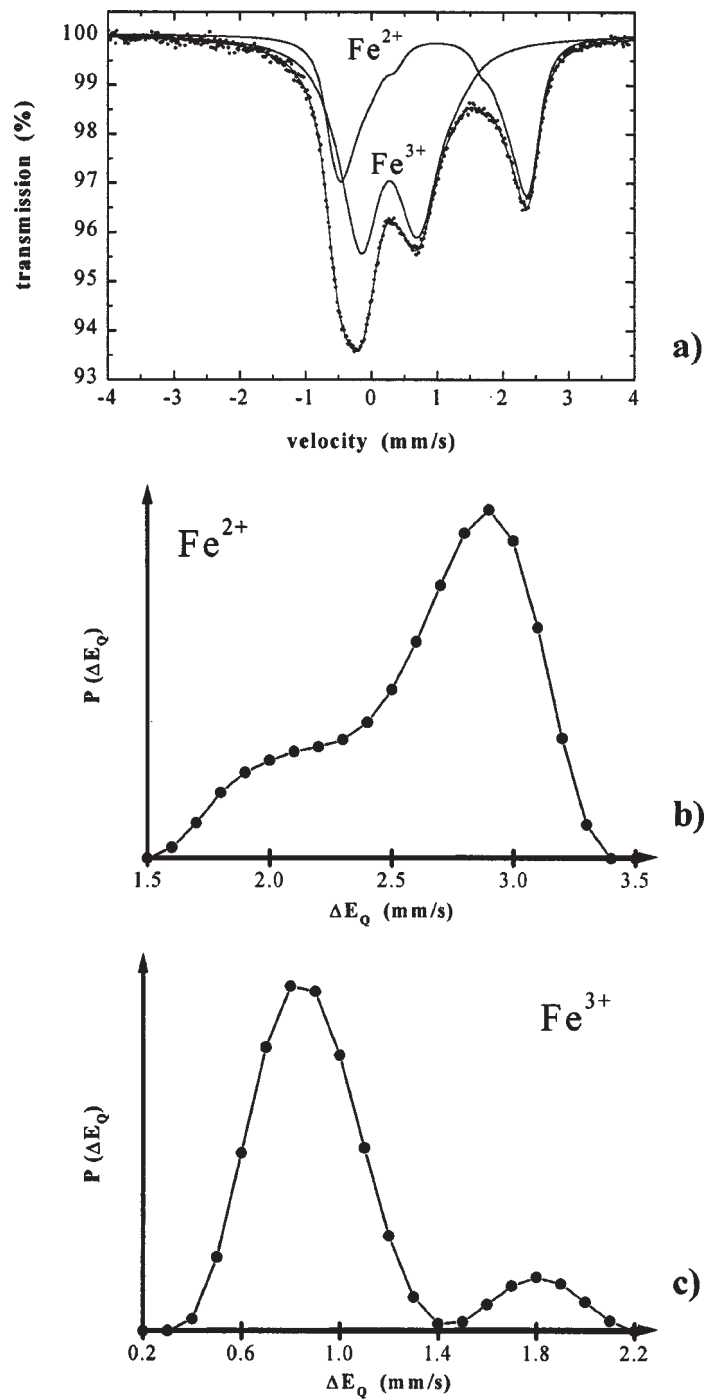
Figure 1. MS spectrum at 80 K of the $Mg_{0.90}Fe_{0.10}Al_2O_4$ oxide powder (a) and quadrupole-splitting distributions of the Fe^{2+} (b) and Fe^{3+} (c) doublets.

Table 1
MS parameters of Fe10MR700, ..., Fe10MR1000 measured at 9 K.

	para Fe^{2+}				ferro α-Fe				
	δ	ΔE_Q	Γ	P	δ	H_{hf}	$2\varepsilon_Q$	Γ	P
Fe10MR700	1.07	2.79	0.65	87	0.17	338	0.03	0.56	13
Fe10MR750	1.07	2.86	0.60	68	0.13	338	0.01	0.46	32
Fe10MR800	1.11	2.70	0.59	30	0.12	337	0.00	0.40	70
Fe10MR850	1.17	2.56	0.43	9	0.12	336	0.00	0.40	91
Fe10MR900	1.19	2.55	0.42	6	0.12	340	0.00	0.33	94
Fe10MR950	–	–	–	–	0.12	338	0.00	0.36	100
Fe10MR1000	–	–	–	–	0.12	340	0.00	0.35	100

Para: paramagnetic; ferro: ferromagnetic; H_{hf}: hyperfine field (kOe); δ: isomer shift (mm s^{-1}); ΔE_Q: quadrupole splitting (mm s^{-1}); $2\varepsilon_Q$: quadrupole shift (mm s^{-1}); Γ: line width (mm s^{-1}); P: proportion (%).

$Mg_{0.90}Fe_{0.10}Al_2O_4$ solid solution will be named Fe10MR1000 and the one obtained by reduction at 1000°C of the attrition-milled $Mg_{0.90}Fe_{0.10}Al_2O_4$ solid solution will be named Fe10AR1000. More generally, one will refer to the M and A powders for composites prepared from mechanically-ground or attrition-milled oxides, respectively.

The XRD patterns of all the composite powders show the presence of α-Fe besides the spinel phase. No Fe^{3+} is detected in the MS spectra even for the lowest T_r (700°C). At 9 K, two spectral components are obvious: a doublet characteristic of paramagnetic Fe^{2+} and a sextet characteristic of ferromagnetic α-Fe. The proportion of Fe^{2+} decreases when T_r increases. In the case of the M powders, no Fe^{2+} is detected for $T_r = 1000$°C regardless of the iron content. The relevant Mössbauer parameters for Fe10MR are listed in table 1 and some typical spectra are shown in figure 2. When T_r increases, the isomer-shift value of the Fe^{2+} doublet increases while the quadrupole-splitting value decreases. This shows a decrease of the electric field gradient around the Fe^{2+} ions, thus a more and more homogeneous environment around these ions. This appears also in the decrease of the peak width of the doublet. The total reduction at 1000°C is confirmed by TGA. Indeed, the weight gain measured for an oxidation in air corresponds to what is expected in the case of a powder containing metallic Fe as the only form of iron. In contrast, incomplete weight gains measured by TGA (figure 3) reveal that the reduction was not complete, even at 1000°C, in the case of the A powders. This could arise because the finer grain size results in more compact A powders, which could limit the diffusion of H_2 inside the powder bed and that of H_2O outside the powder bed and therefore hampers the reduction process.

Above 50 K, a singlet appears on the MS spectra. The MS spectrum of Fe10MR1000 at RT is shown in figure 4(a) as a typical example. The spectrum of the latter powder was also recorded at 275 K under an external magnetic field of 60 kOe applied parallel to the γ-beam (figure 4(b)). The MS parameters with and without field are given in table 2. The external-field spectrum is composed of two quadruplets (fixed area ratio 3 : 0 : 1) characteristic of ferromagnetic α-Fe and of a paramagnetic phase,
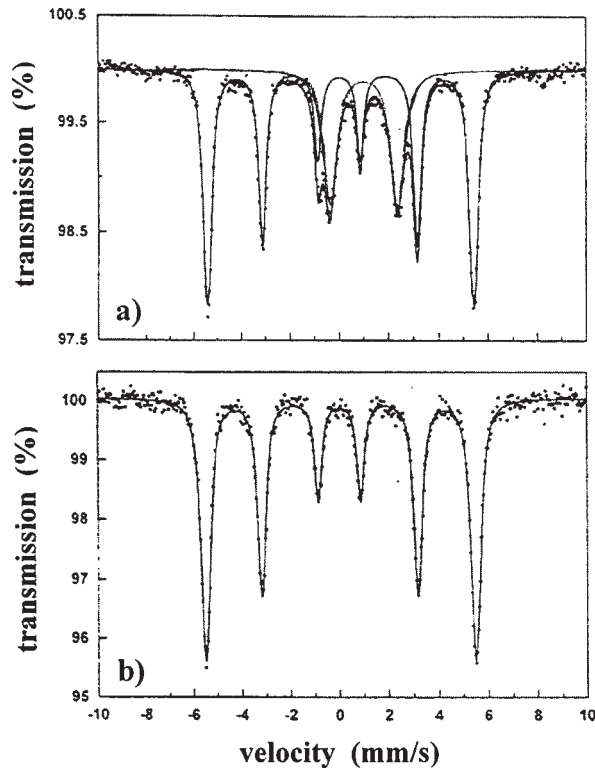
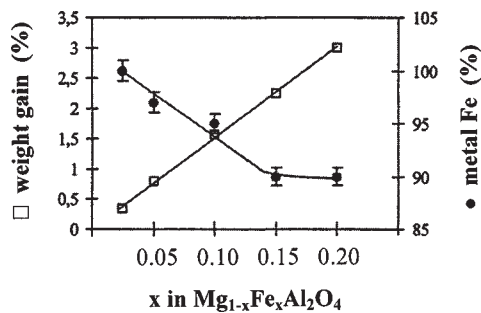Figure 2. MS spectra at 9 K of Fe10MR800 (a) and Fe10MR1000 (b).

Figure 3. Proportion of metallic iron versus the iron content in the A nanocomposite powders. The percentage of metallic iron refers to the total iron weight in the specimen. The lines are guides to the eye.

respectively. The hyperfine field of the latter quadruplet is equivalent to the applied external field. Moreover, the proportion of this quadruplet is the same as that of the singlet detected without applied field. The singlet above 50 K was thus attributed to a paramagnetic α-Fe phase due to extremely small particles with very low Curie temperature.

The DTG curves of Fe10MR1000 (a) and Fe10AR1000 (b) are shown in figure 5. In the case of Fe10MR1000, the oxidation of the Fe particles proceeds in three stages
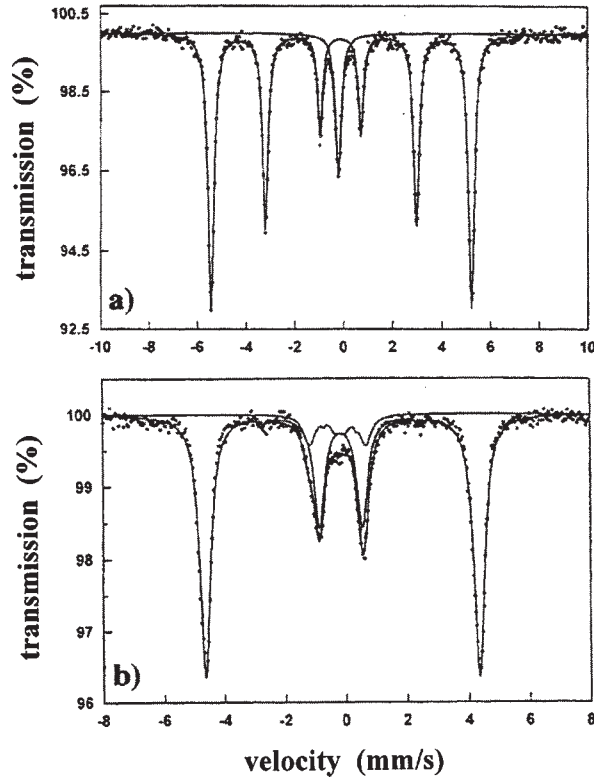
Figure 4. MS spectra of Fe10MR1000 measured at RT (a) and measured at 275 K in an external magnetic field of 60 kOe applied parallel to the γ-beam (b).

Table 2
MS parameters of Fe10MR1000 measured at RT and measured at 275 K in an external magnetic field of 60 kOe applied parallel to the γ-beam.

H_{ext}	ferro α-Fe					non-ferro Fe				
	δ	H_{hf}	$2\varepsilon_Q$	Γ	P	δ	H_{hf}	$2\varepsilon_Q$	Γ	P
0	0.01	331	0.00	0.28	89	−0.07	–	–	0.30	11
60	−0.03	279	0.00	0.43	89	−0.09	58	0.08	0.41	11

Ferro: ferromagnetic; H_{ext}: applied external magnetic field (kOe); H_{hf}: hyperfine field (kOe); δ: isomer shift (mm s^{-1}); $2\varepsilon_Q$: quadrupole shift (mm s^{-1}); Γ: line width (mm s^{-1}); P: proportion (%).

designated S1 (295°C), S2 (475°C) and S3 (780°C). In the case of Fe10AR1000, the oxidation process evaluates in only two stages, corresponding to S1 and S3. A treatment of the powders in HCl (boiling, 1 mol/l) was performed prior to the TGA measurements. For these treated powders, the steps S1 and S2 are not detected whereas S3 remains unchanged. In agreement with earlier studies [12,16] this behavior shows that the Fe particles corresponding to S1 and S2 are located on the surface of the matrix grains
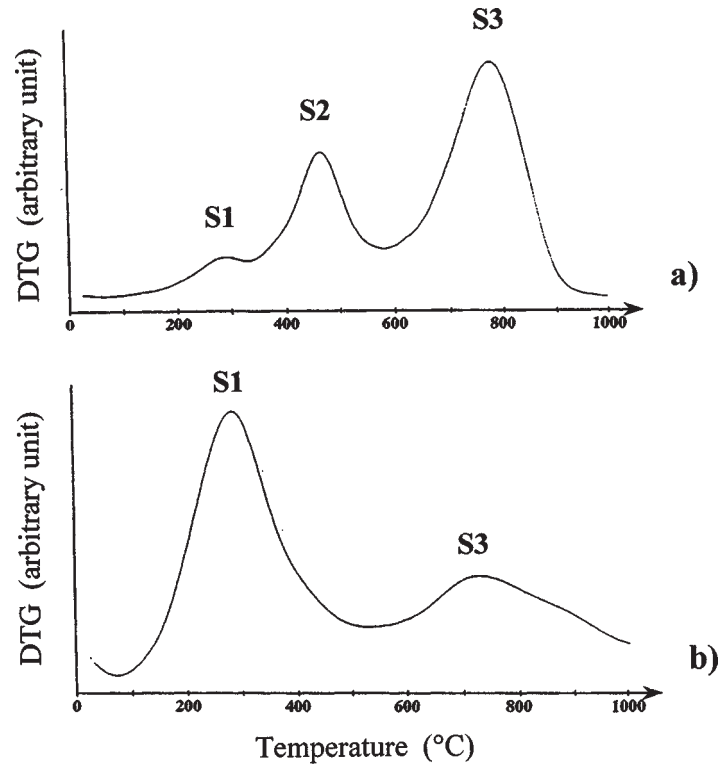
Figure 5. DTG patterns of Fe10MR1000 (a) and Fe10AR1000 (b).

or inside its open porosity, whereas those related to S3 are embedded inside the oxide grains and are therefore protected against the acid treatment.

To obtain a better understanding of the microstructure of the powders, the specimen Fe10MR1000 was oxidized in air at 300°C (powder T300), 500°C (T500) and 900°C (T900), these temperatures corresponding to the oxidation stages S1, S2 and S3, respectively. The MS spectra were recorded at RT (figure 6 and table 3). For T300, a doublet characteristic of paramagnetic Fe^{2+} is detected besides paramagnetic (singlet) and ferromagnetic (sextet) α-Fe. No separate iron oxide phase is detected in the XRD pattern of T300, which indicates that the Fe^{2+} ions are substituted in the spinel lattice. Since the proportion of paramagnetic α-Fe has remained unchanged, compared to that for Fe10MR1000, and that of ferromagnetic α-Fe is lower, S1 is assigned to the oxidation of small ferromagnetic α-Fe particles located on the surface or in the open porosity of the matrix grains. For T500, the singlet has the same proportion, indicating that the corresponding particles were not oxidized and therefore that these particles are those located inside the matrix grains. This agrees with the hypothesis that this phase corresponds to the smallest particles. Two doublets characteristic of Fe^{2+} ions in the spinel lattice are detected. The sum of their proportions corresponds to the proportion of Fe^{2+} detected in T300. The proportion of the sextet of α-Fe still decreases in favor of a sextet
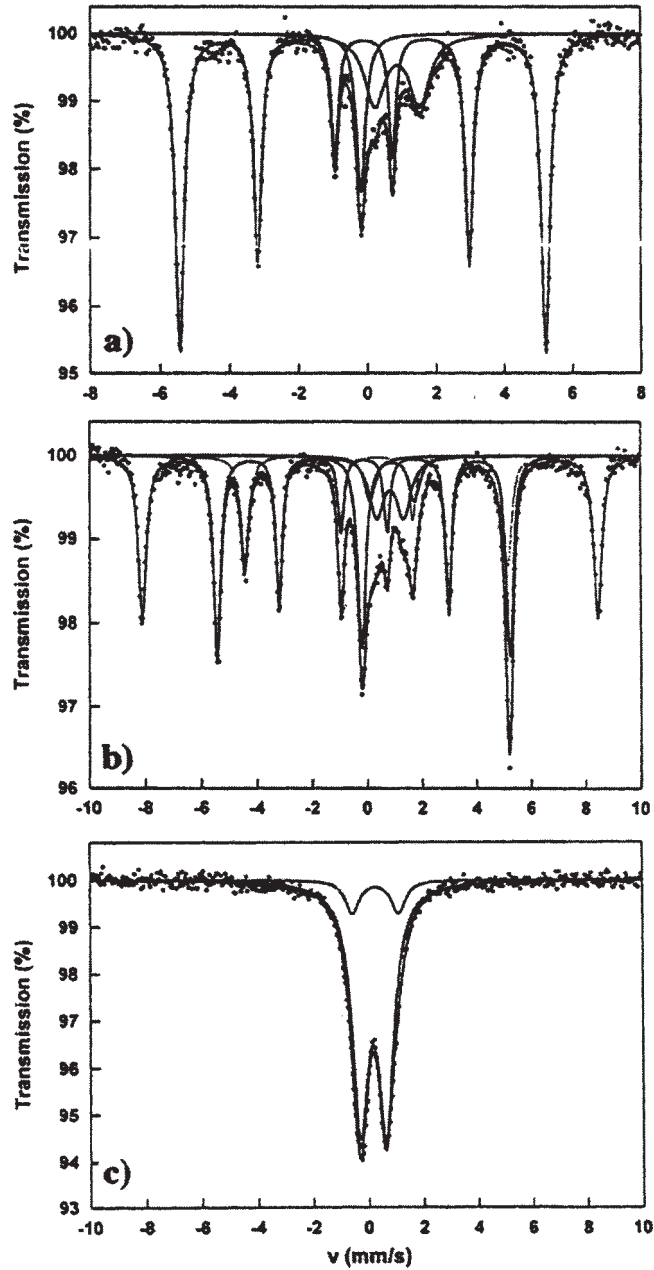
Figure 6. MS spectra at RT of Fe10MR1000 after oxidation and quenching in air at 300°C (a), 500°C (b) and 900°C (c).

of α-Fe_2O_3. S2 is thus attributed to the oxidation of relatively large Fe particles located on the surface of the matrix grains. Finally, T900 presents two doublets characteristic of Fe^{3+} ions located in the octahedral and tetrahedral sites of the spinel lattice. The ox-

Table 3
MS parameters of T300, T500 and T900 measured at RT.

	ferro α-Fe					para α-Fe		
	δ	H_{hf}	$2\varepsilon_Q$	Γ	P	δ	Γ	P
T300	0.01	330	0.01	0.28	72	−0.07	0.32	10
T500	0.00	330	0.02	0.28	37	−0.09	0.36	10
T900	–	–	–	–	–	–	–	–

	α-Fe$_2$O$_3$					para Fe^{2+}				para Fe^{3+}			
	δ	H_{hf}	$2\varepsilon_Q$	Γ	P	δ	ΔE_Q	Γ	P	δ	ΔE_Q	Γ	P
T300	–	–	–	–	–	0.99	1.30	0.70	18	–	–	–	–
T500	0.37	514	−0.18	0.28	37	1.02	1.62	0.48	7	–	–	–	–
						0.95	0.98	0.64	11	–	–	–	–
T900	–	–	–	–	–	–	–	–	–	0.37	1.68	0.69	89
										0.27	0.93	0.60	11

Ferro: ferromagnetic; para: paramagnetic; H_{hf}: hyperfine field (kOe); δ: isomer shift (mm s^{-1}); ΔE_Q: quadrupole splitting (mm s^{-1}); $2\varepsilon_Q$: quadrupole shift (mm s^{-1}); Γ: line width (mm s^{-1}); P: proportion (%).
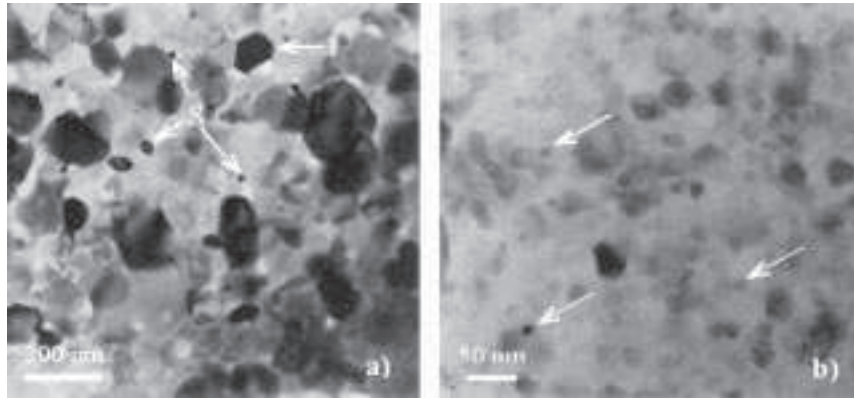

Figure 7. TEM images of Fe10MR1000 (a) and Fe10AR1000 (b). S stands for small metal particles and L for large metal particles.

idation is thus complete and all the Fe ions have migrated to the oxide lattice forming a lacunar spinel.

TEM observations are in good agreement with these results. Indeed the image of Fe10MR1000 (figure 7(a)) shows metallic particles smaller than 30 nm in diameter and larger ones ca. 200 nm in diameter. In the case of Fe10AR1000, only particles smaller than 30 nm are observed. A typical image is shown in figure 7(b). Figure 8 shows the evolution of the proportions of S1, S2 and S3 versus the iron content in the powders. In the case of the M powders (figure 8(a)), the proportion of Fe dispersed as small surface particles (S1) is constant whereas that of Fe dispersed as larger surface particles (S2) increases and that of intragranular Fe (S3) decreases. In the case of the A powders
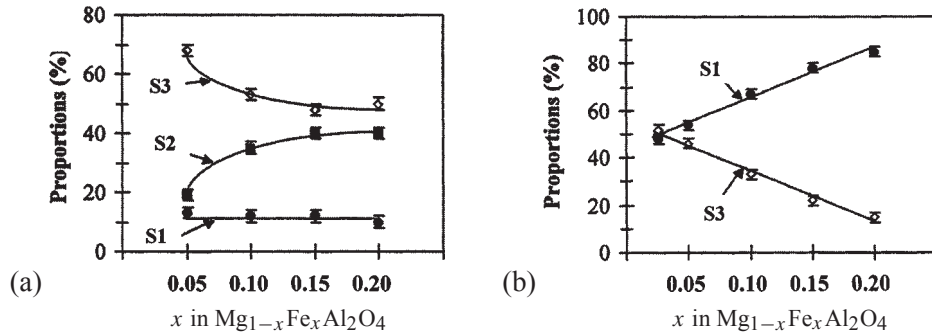
Figure 8. Proportions of α-Fe versus the iron content in the M (a) and A (b) nanocomposite powders: SI refers to α-Fe in the form of small particles outside the matrix grains, S2 refers to α-Fe in the form of large particles outside the matrix grains and S3 refers to α-Fe in the form of particles inside the matrix grains. The lines are guides to the eye.

(figure 8(b)), a higher amount of iron results in more Fe surface particles (S1). The proportion of surface Fe is always higher for the A powders (ca. 50–85%) than for the M ones (ca. 30–50%). It is noteworthy that despite this, large Fe surface particles (S2) are apparently not present in the A powders.

3.3. Fe/Co– and Fe/Ni–MgAl$_2$O$_3$ powders

The $Mg_{0.90}Fe_{0.065}Co_{0.035}Al_2O_4$ and $Mg_{0.90}Fe_{0.065}Ni_{0.035}Al_2O_4$ mechanically-ground solid solutions were reduced in H_2 ($700 \leqslant T_r \leqslant 1000°C$, 1 h). For the sake of briefness, the resulting nanocomposite powders will hereafter be denoted as FeCoR700, FeCoR750, ..., FeNiR1000.

The XRD patterns of the composite powders reveal the presence of a spinel as the major phase. The bcc Fe/Co (1 1 0) peak cannot be resolved because of its superposition with the (4 0 0) spinel peak, but an examination of the evolution of the intensity of the corresponding peak versus that of the (3 1 1) spinel peak reveals the evolving formation of bcc Fe/Co alloy(s) and suggests that the reduction of the transition-metal ions is completed at 900°C. The γ-Fe/Ni (1 1 1) and (2 0 0) peaks are clearly detected in the XRD patterns. Their intensities increase with increasing T_r, but the reduction of the transition metal ions is not completed below 1000°C.

TEM observations reveal metal nanoparticles homogeneously dispersed in the oxide matrix (figure 9). The number of particles is higher in the R900 and R1000 composites than in R700 and R800 specimens. In all cases, the size distributions are monomodal and rather narrow. Previous works [5,8] have shown that this mainly results from the monophased nature of the starting oxide solid solutions. The average size of the metal particles increases with increasing T_r, from 6.3 to 12.5 nm for FeCoR700 and FeCoR1000, respectively, and from 6.5 to 10.1 nm for FeNiR700 and FeNiR1000, respectively. EDX examinations show that an increase in T_r leads to a more narrow composition distribution and to an average composition ($Fe_{0.63}Co_{0.37}$ for FeCoR1000 and $Fe_{0.64}Ni_{0.36}$ for FeNiR1000) closer to the desired one ($Fe_{0.65}Mo_{0.35}$, M = Co or Ni).
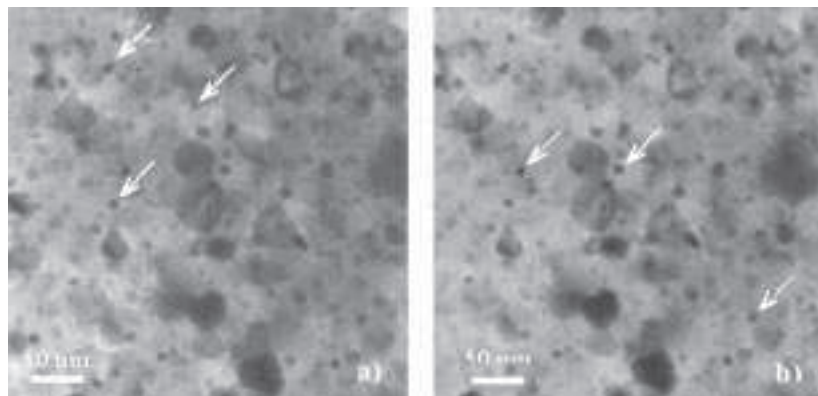
Figure 9. TEM images of FeCoR1000 (a) and FeNiR1000 (b). Some metal particles, appearing as small dark dots, are pointed out by arrows. Some larger dark areas are probably matrix grains in or near the Bragg position with respect to the electron beam.

The particles become Fe-richer with the increase in T_r, showing that the Co^{2+} and Ni^{2+} ions are more easily reducible than the Fe^{2+} ions.

The MS spectra of the Fe/Co– (table 4) and Fe/Ni–$MgAl_2O_4$ (table 5) powders obtained after reduction at 700, 800, 900 and 1000°C were recorded at 9 K. Figure 10 presents the spectra of FeCoR800 (a), FeCoR1000 (b), FeNiR800 (c, e) and FeNiR1000 (d, f). They were fitted with a doublet representing paramagnetic Fe^{2+} ions and a sextet accounting for ferromagnetic Fe/Co or Fe/Ni alloys. Fe^{3+} ions were not detected, showing that the reduction to the ferrous state is complete at a temperature below 700°C. The Fe^{2+} doublet proportion decreases with increasing T_r, reaching 0% for FeCoR900 and FeNiR1000, in line with the XRD results. This shows that the reduction of Co^{2+} ions promotes the Fe^{2+} ions reduction more efficiently than the reduction of Ni^{2+} ions does. The Fe/Co particles, the proportion of which accordingly increases with T_r, exhibit the same value for the hyperfine field although their composition is slightly different from one composite to the other. This is in agreement with a study by Johnson et al. [40] revealing a nearly constant hyperfine-field value ($H_{hf} = 365$ kOe) in the $Fe_{0.80}Co_{0.20}$–$Fe_{0.65}Co_{0.35}$ composition range. No ferromagnetic α-Fe/Ni is detected, showing that the martensitic γ–α transformation upon cooling is suppressed in fine alloy particles containing more than 20 at.% Ni, as indicated on the Fe–Ni phase diagram [41]. The hyperfine-field distribution $P(H_{hf})$ of the Fe/Ni sextets is broad, ranging between 250 and 400 kOe (figure 10(e,f)). The distributions show several peaks, the number and positions of which depend upon T_r. Similar line shapes have been reported by several authors for ferromagnetic γ-Fe/Ni alloys [42–46]. Since the Ni content is known to have a strong influence on the hyperfine field of the corresponding sextets [40], the observed field-distribution line shapes in the present Fe/Ni alloys could reflect compositional fluctuations, as suggested by the EDX results.

The MS spectra of the FeCoR1000 (a) and FeNiR1000 (b, c) composites have also been recorded at RT (figure 11). FeCoR1000 presents only a sextet ($H_{hf} = 365$ kOe),

Table 4
MS parameters of FeCoR700, FeCoR800, FeCoR900 and FeCoR1000 measured at 9 K.

| | para Fe^{2+} | | | | ferro Fe/Co | | | | |
	δ	ΔE_Q	Γ	P	δ	H_{hf}	$2\varepsilon_Q$	Γ	P
FeCoR700	1.05	2.86	0.55	84	0.12	367	0.00	0.30	16
FeCoR800	1.04	2.78	0.57	9	0.14	366	0.00	0.34	91
FeCoR900	–	–	–	–	0.15	366	0.00	0.36	100
FeCoR1000	–	–	–	–	0.15	367	0.00	0.36	100

Para: paramagnetic; ferro: ferromagnetic; H_{hf}: hyperfine field (kOe); δ: isomer shift (mm s^{-1}); ΔE_Q: quadrupole splitting (mm s^{-1}); $2\varepsilon_Q$: quadrupole shift (mm s^{-1}); Γ: line width (mm s^{-1}); P: proportion (%).

Table 5
MS parameters of FeNiR700, FeNiR800, FeNiR900 and FeNiR1000 measured at 9 K.

| | para Fe^{2+} | | | | ferro Fe/Ni | | | | |
	δ	ΔE_Q	Γ	P	δ	H_{hf}	$2\varepsilon_Q$	Γ	P
FeNiR700	1.22	2.62	0.61	60	0.17	333	0.01	0.96	40
FeNiR800	1.22	2.70	0.45	15	0.18	337	0.02	0.46	85
FeNiR900	1.15	2.61	0.41	5	0.18	350	0.01	0.41	95
FeNiR1000	–	–	–	–	0.18	346	0.00	0.47	100

Para: paramagnetic; ferro: ferromagnetic; H_{hf}: hyperfine field (kOe); δ: isomer shift (mm s^{-1}); ΔE_Q: quadrupole splitting (mm s^{-1}); $2\varepsilon_Q$: quadrupole shift (mm s^{-1}); Γ: line width (mm s^{-1}); P: proportion (%).

representing ferromagnetic bcc Fe/Co alloy(s). FeNiR1000 shows a sextet accounting for ferromagnetic Fe/Ni alloy(s) and a singlet, the area of which represents 20% of the total spectrum. The value of the average hyperfine field of the sextet (300 kOe) confirms that the composition of the particles obtained after reduction at 1000°C is close to the desired one (Fe$_{0.65}$Ni$_{0.35}$) [40,44,47]. The field distribution is broad (figure 11(c)), ranging between 200 and 340 kOe, with a peak at about 300 kOe and a strong shoulder on the low-H_{hf} side (ca. 240 kOe). It is probable that the shoulder and peak correspond to those observed on the 9 K data plot at about 290 and 340 kOe, respectively.

The presence of a singlet at RT reflects the presence of a phase which is non-ferromagnetic. In order to get more information on this singlet, FeNiR1000 was measured at 275 K in a 60 kOe external magnetic field applied parallel to the γ-beam (figure 12). The best fit was obtained assuming that two quadruplets (fixed area ratio 3 : 0 : 1) compose the total spectrum. The first quadruplet ($H_{hf} = 258$ kOe) represents the ferromagnetic γ-Fe/Ni phase. The second one ($H_{hf} = 45$ kOe) is consistent with a paramagnetic γ-Fe/Ni phase and its proportion (20%) corresponds to that of the singlet in the spectrum recorded without applied field.

Similar spectra have earlier been reported for γ-Fe/Ni alloys with 30, 32 and 34 at.% of Ni, from RT down to liquid-N$_2$ temperature [48]. These authors concluded that the singlet may originate from antiferromagnetic regions, the Néel temperature of
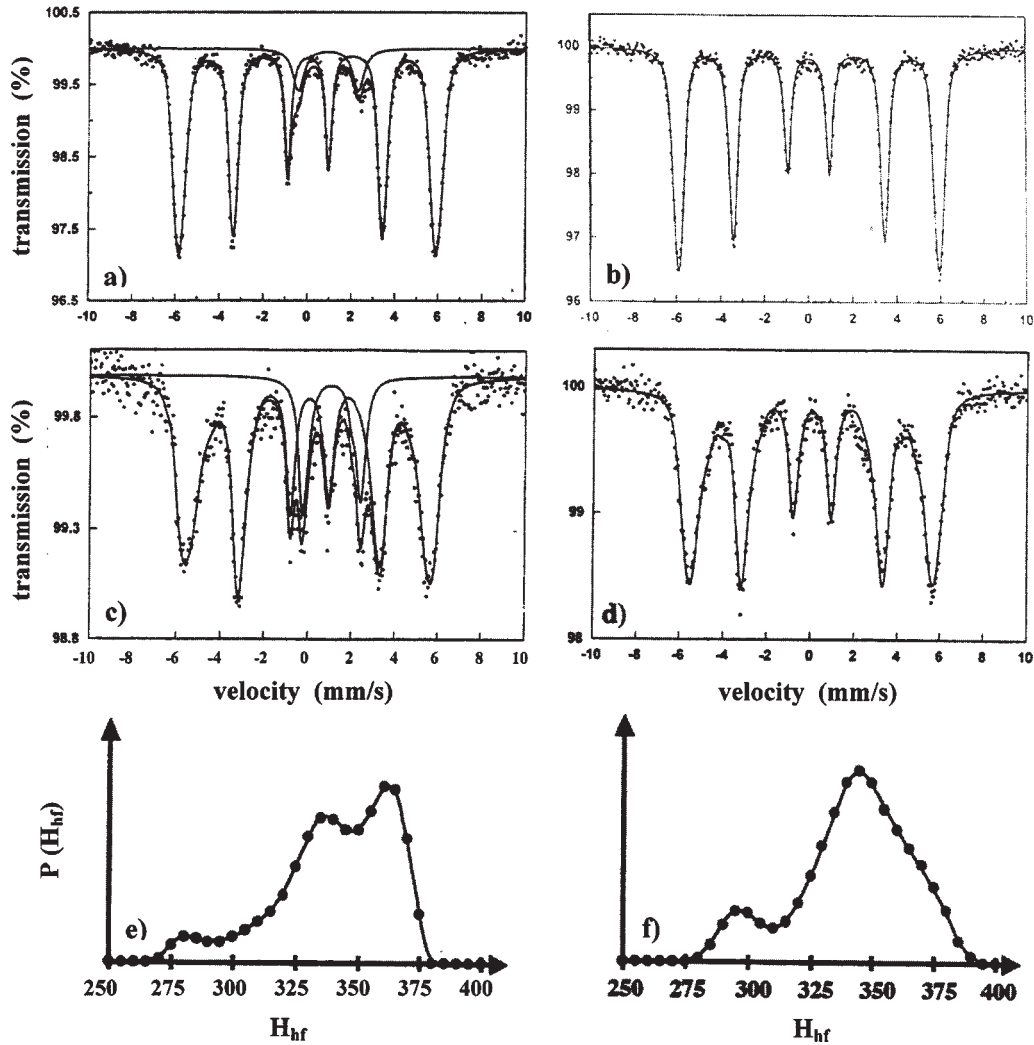
Figure 10. MS spectra at 9 K of FeCoR800 (a), FeCoR1000 (b), FeNiR800 (c), FeNiR1000 (d) and hyperfine-field distributions for FeNiR800 (e) and FeNiR1000 (f).

which may be well below liquid-N_2 temperature. Several models [45,47,49–51] have been proposed to explain the origin of these antiferromagnetic regions in γ-Fe/Ni Invar alloys. However, the existence of two states of the iron atoms [47,51] can be ruled out in the present study because the MS spectrum of FeNiR1000 recorded at 9 K (figure 10(d)) shows only one sextet representative of a ferromagnetic alloy. According to Kachi and Asano [50], paramagnetism could also appear due to fluctuations of the local Ni concentration around a critical value in the 30–35 at.% range content. In the present case, one has to consider the fluctuations from one alloy particle to the other, on the one hand, and within a given alloy particle, on the other hand. In the latter case, one may
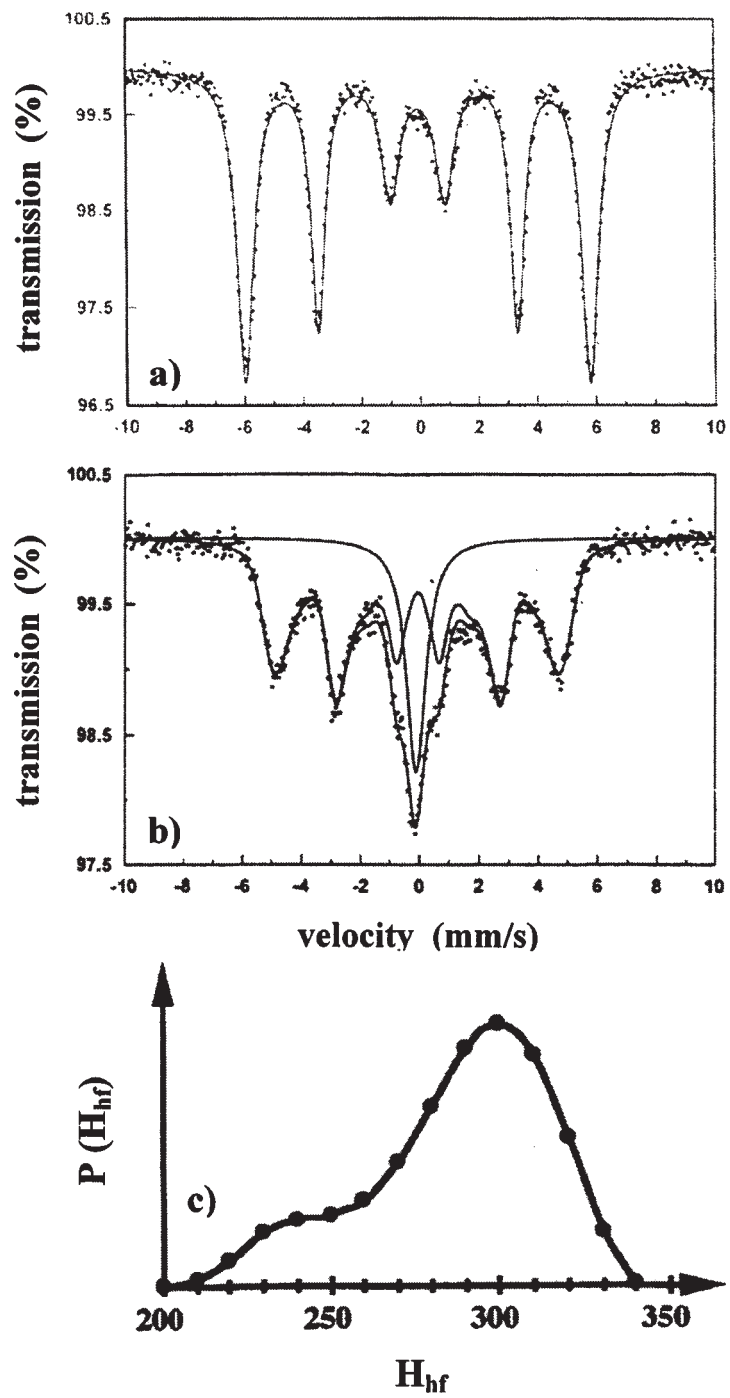
Figure 11. MS spectra at RT of FeCoR1000 (a), FeNiR1000 (b) and hyperfine-field distribution for FeNiR1000 (c).
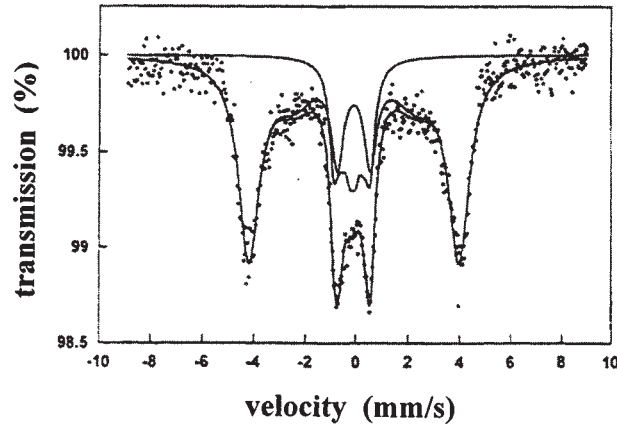
Figure 12. MS spectrum of FeNiR1000 measured at 275 K in a 60 kOe external magnetic field applied parallel to the γ-beam.

assume that the surface alloy particles, which are formed first, are more homogeneous than the intragranular ones, for which the slight differences in reduction temperatures for Ni^{2+} and Fe^{2+} could have provoked a composition gradient. Thus, the intragranular particles would have a Ni-rich internal part and a Fe-rich external part, leading to the ferromagnetic and paramagnetic behaviors, respectively.

It was revealed by TGA that ca. 87% of the metallic phase in FeNiR1000 is dispersed as intragranular particles. The surface Fe/Ni particles were removed by a treatment of the composite powder in HCl and the MS spectrum of the resulting material, representative for the intragranular Fe/Ni alloy particles only, was recorded at RT. The best fit was obtained assuming that the MS spectrum is composed of a sextet (average $H_{hf} = 300$ kOe, 89%) characteristic of ferromagnetic $Fe_{0.65}Ni_{0.35}$ alloy and a singlet $\delta = 0.00$ mm s^{-1}, 11%) accounting for paramagnetic Fe/Ni. Combining the MS proportions for the untreated and HCl-treated powder and those obtained by TGA gives a rough estimation of the proportions of the different Fe species with respect to the total metal content. Indeed, we find that the ferromagnetic and paramagnetic surface Fe account for 3 and 10%, respectively, whereas the ferromagnetic and paramagnetic intragranular Fe account for 77 and 10%, respectively. The paramagnetic particles are evenly distributed at the surface of the matrix grains and inside them and there is a very high proportion of the ferromagnetic intragranular Fe. Since the intragranular particles are generally smaller than the surface ones, these results imply that the RT paramagnetism is not based on a size effect, because one would then have observed a majority of paramagnetic intragranular metal particles. Furthermore, the large amount of ferromagnetic intragranular Fe is inconsistent with the hypothesis that concentration fluctuations within individual particles are the main cause of RT paramagnetism. Thus, this phenomenon was attributed to composition fluctuations from one alloy particle to the other.

3.4. CNTs–Fe/Fe₃C–MgAl₂O₄ powders

The $Mg_{1-x}Fe_xAl_2O_4$ spinel solid solutions ($0.10 \leqslant x \leqslant 0.40$) were reduced in H_2/CH_4 at 1070°C for 6 min [31]. The oxides used in this study were attrition-milled. Indeed, as noted in section 3.2, this favors a higher proportion of metal at the surface of the oxide grains while avoiding an exaggerated growth of the particles. The nanocomposite powders in this section will be referred to as in the following example: Mg9Fe1R will designate the powder reduced from $Mg_{0.90}Fe_{0.10}Al_2O_4$.

The XRD patterns of the composite powders reveal the presence of α-Fe and Fe_3C in addition to the spinel matrix. However, no γ-Fe can be resolved, possibly due to the superposition of its peaks with those of the major phases [31]. SEM observations reveal that the metal–oxide grains are uniformly covered by a web-like network of CNTs bundles, several tens of micrometers long (figure 13(a)). TEM observations show that these bundles are made up of single-wall (SWNTs) and thin multi-wall (MWNTs) nanotubes with a diameter close to 4 nm (figure 13(b)).

The total carbon content in the powders increases almost linearly with the amount of iron (figure 14(a)). Using the macroscopical characterization method described above, it appears that the quantity of CNTs strongly increases between Mg9Fe1R and Mg8Fe2R, reaching saturation for Mg7Fe3R (figure 14(b)). The evolution between Mg9Fe1R and Mg8Fe2R could reflect the higher density of potentially active particles at the surface of the matrix grains upon the increase of the total iron content. For specimens with a higher iron content (Mg7Fe3R and Mg6Fe4R), this is balanced by an easier coalescence, and hence deactivation, of the surface particles. In all cases, an increase in iron content produces larger particles on the surface. The formation of thicker CNTs is then reflected in the evolution of the quality factor which gradually decreases from Mg9Fe1R to Mg6Fe4R (figure 14(c)).

The MS parameters at 80 K of the nanocomposite powders are reported in table 6 and the MS spectra at 80 K of Mg9Fe1R and Mg6Fe4R are shown in figure 15. Three phases are detected: a sextet characteristic of ferromagnetic α-Fe, a sextet characteristic
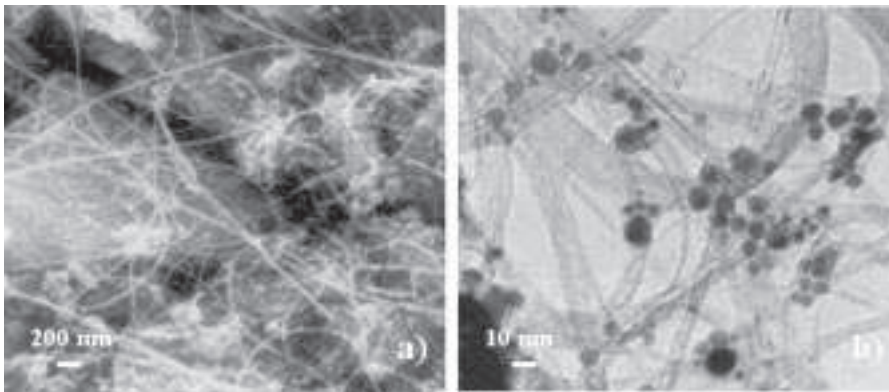

Figure 13. SEM (a) and TEM (b) images of the Mg8Fe2R nanocomposite powder.

of ferromagnetic Fe_3C [53] and a singlet characteristic of a paramagnetic phase. The three phases appear with the same proportions at all temperatures, but the singlet shows a clear broadening at low temperatures. For measuring temperatures below 80 K, a better fit is obtained using a weak sextet instead of a singlet for the central part of the spectrum. Figure 16 shows the MS spectrum of Mg9Fe1R measured at 4 K. The sextet
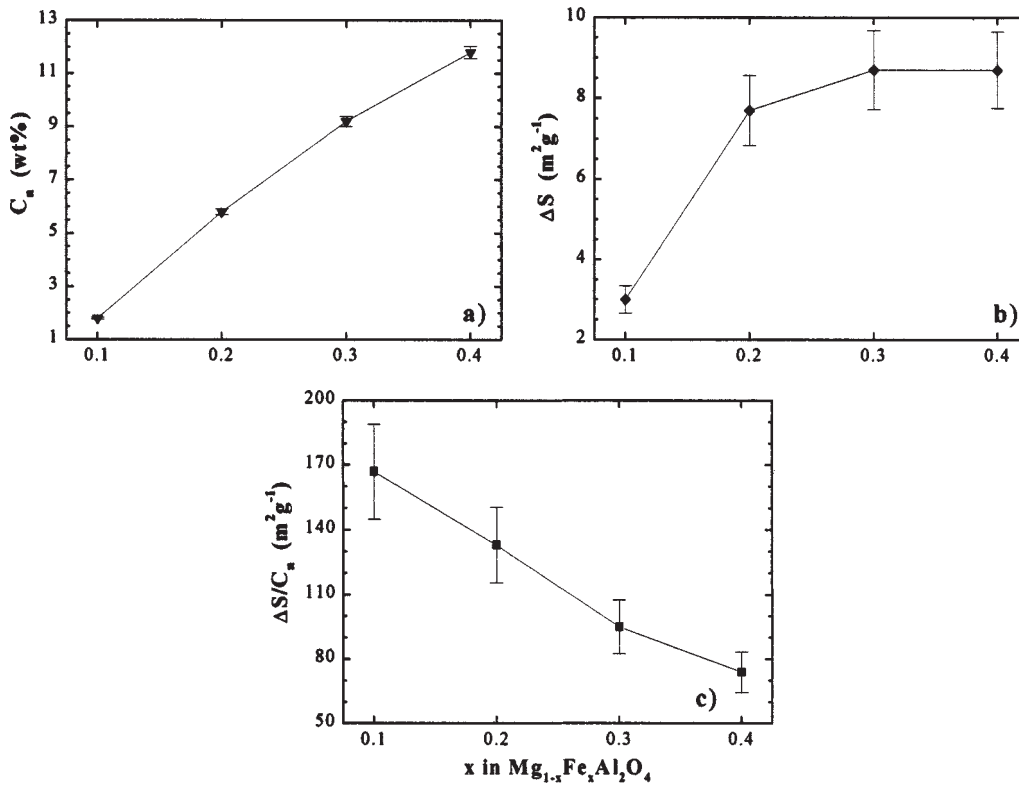

Figure 14. Carbon content (C_n) (a), quantity factor (ΔS) of the CNTs (b) and quality factor ($\Delta S/C_n$) of the CNTs (c) versus the iron content in the nanocomposite powders. The lines are guides to the eye.

Table 6
MS parameters of Mg9Fe1R, Mg8Fe2R, Mg7Fe3R and Mg6Fe4R measured at 80 K.

	ferro α-Fe					ferro Fe_3C					non-ferro Fe		
	δ	H_{hf}	$2\varepsilon_Q$	Γ	P	δ	H_{hf}	$2\varepsilon_Q$	Γ	P	δ	Γ	P
Mg9Fe1R	0.12	342	0.00	0.31	44	0.30	247	$\sim$0	0.34	31.5	0.04	0.58	24.5
Mg8Fe2R	0.12	343	0.00	0.29	27.5	0.31	248	$\sim$0	0.32	59	0.03	0.51	13.5
Mg7Fe3R	0.11	342	0.00	0.28	21.5	0.31	247	$\sim$0	0.31	62.5	0.02	0.40	16
Mg6Fe4R	0.11	340	0.00	0.29	21	0.31	247	$\sim$0	0.31	54	0.02	0.36	25

Ferro: ferromagnetic; H_{hf}: hyperfine field (kOe); δ: isomer shift (mm s^{-1}); $2\varepsilon_Q$: quadrupole shift (mm s^{-1}); Γ: line width (mm s^{-1}); P: proportion (%).
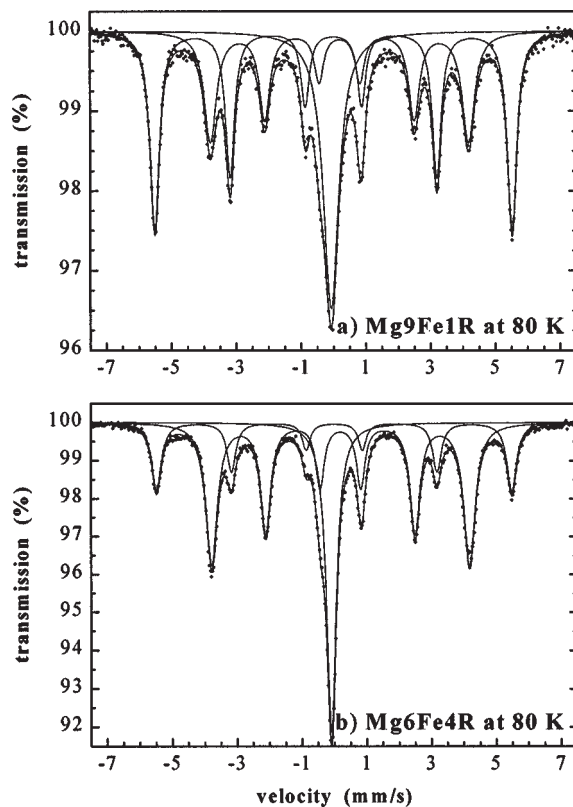
Figure 15. MS spectra at 80 K of Mg9Fe1R (a) and Mg6Fe4R (b).

used for the central part has a hyperfine field of 18.5 kOe. This could indicate that the corresponding Fe-species undergo a paramagnetic–antiferromagnetic transformation whose transition temperature is found to be about 75 K. This suggests a γ-Fe phase since it is known that the spins in γ-Fe show an antiferromagnetic coupling below 80 K [47]. A saturation hyperfine field of 27 ± 5 kOe was reported for small antiferromagnetic γ-Fe–Ni particles [52], which is in good agreement with the hyperfine fields found in this study.

Comparing these results to those obtained for Fe–MgAl$_2$O$_4$ nanocomposite powders, it is proposed that the singlet, still present at a temperature as low as 4 K with an unchanged proportion, could reflect the formation of a γ-Fe–C phase. Indeed, a small proportion of carbon could hinder the γ–α transformation. The absence in the present spectra of the paramagnetic α-Fe phase detected for Fe–MgAl$_2$O$_4$ powders may indicate that at least a part of the corresponding intragranular particles are found in the form of γ-Fe–C species in the CNTs–Fe/Fe$_3$C–MgAl$_2$O$_4$ materials. A study on CNTs–Fe/Fe$_3$C–Al$_2$O$_3$ composite powders [32] has indeed shown that γ-Fe (possibly γ-Fe–C) species were located in intragranular position. This could indicate that a fraction of the carbon supplied by the decomposition of CH$_4$ migrates inside the lattice of the oxide matrix.
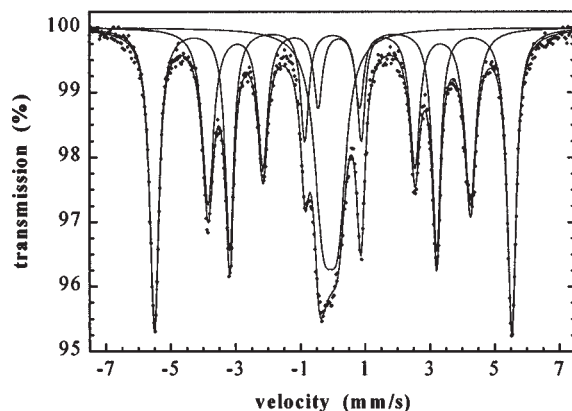
Figure 16. MS spectrum at 4 K of Mg9Fe1R.

The proportions of the different iron phases present in the composite powders are shown in figure 17(a). The proportion of Fe_3C roughly doubles from ca. 30 to ca. 60% between Mg9Fe1R and Mg8Fe2R and then reaches a plateau. The fraction of α-Fe follows an almost opposite evolution whereas the γ-Fe–C proportion initially decreases and then increases again so that it is similar for Mg9Fe1R and Mg6Fe4R. Figure 17(b) shows the amounts of the different Fe phases present in the samples. To obtain a reasonable approximation of the amounts from the proportions, the latter were multiplied by 1, 2, 3 and 4 for Mg9Fe1R, Mg8Fe2R, Mg7Fe3R and Mg6Fe4R, respectively. The contents of both Fe_3C and α-Fe steadily increase with the iron content, the former one in a much more pronounced way. In contrast, the γ-Fe–C content is the same for Mg9Fe1R and Mg8Fe2R and only increases for higher amounts of iron. Comparing these results to the evolution of the CNTs-quantity factor (figure 14(b)), it appears that the particles responsible for the nucleation and possibly for the growth of the CNTs are found in the form of Fe_3C in the post-reaction MS analysis. However the exact nature of the catalytic particle at the temperature of the reaction is not known, but it is probably a very small carbon-containing Fe particle where some still poorly-established driving forces make carbon atoms participate in the formation of the CNTs. However, the continuous increase of the Fe_3C quantity indicates that some of the particles located at the surface of the spinel grains that were inactive for the formation of the CNTs also end up as cementite. The continuous increase of the quantities of α-Fe and γ-Fe–C could also indicate that such inactive particles are detected as α-Fe and γ-Fe–C in post-reaction Mössbauer spectra.

The Mg9Fe1R powder was oxidized in air at 600°C for 2 h. This thermal treatment is thought [12,38] to result in the oxidation of all the metal or carbide particles located on the surface of the matrix grains, whereas the intragranular particles should remain unoxidized. This product will be referred to as Mg9Fe1RO. Figure 18 shows the MS spectra of Mg9Fe1RO measured at RT (a) and at 80 K (b). The MS parameters are given in table 7. Compared to the corresponding MS spectra of Mg9Fe1R, the sextet of Fe_3C has become very weak but α-Fe and γ-Fe–C are still clearly detected. In addition, four oxide phases are detected: magnetic α-Fe$_2$O$_3$, ferrimagnetic $MgFe_2O_4$, paramagnetic
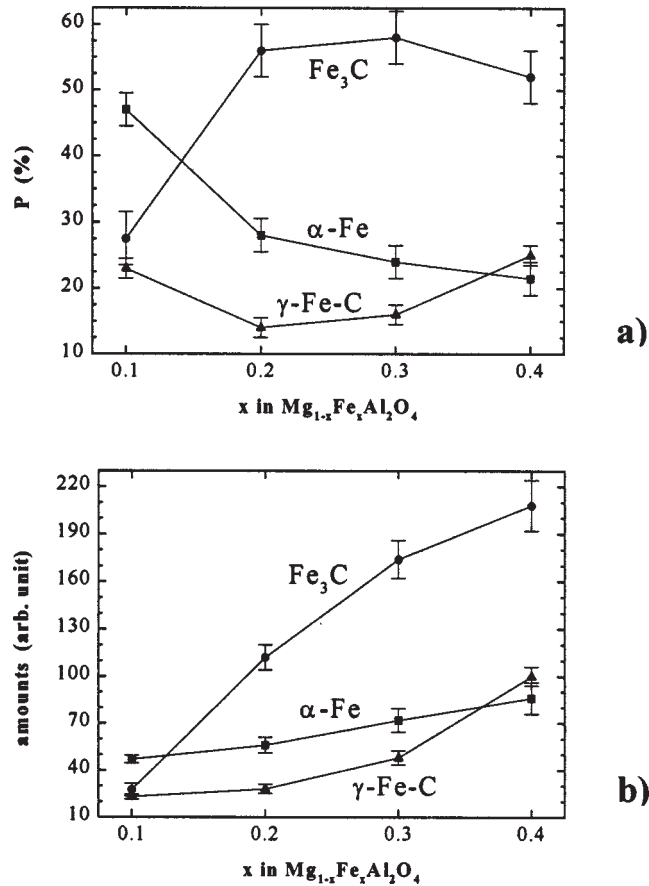
Figure 17. Proportions of the different iron phases present in the nanocomposite powders as revealed by MS (a) and corresponding amounts of the different Fe phases in the powders (b). The amounts were obtained by multiplying the corresponding proportions by 1, 2, 3 and 4 for Mg9Fe1R, Mg8Fe2R, Mg7Fe3R and Mg6Fe4R, respectively. The lines are guides to the eye.

Fe^{2+} and paramagnetic Fe^{3+}. α-Fe and γ-Fe–C corresponds to intragranular particles that were not oxidized. At 80 K, the proportion of Fe^{3+} decreases in favor of α-Fe_2O_3 and $MgFe_2O_4$, while the proportion of Fe^{2+} remains constant. The results presented in section 3.2 have shown that for an oxidation temperature of 600°C, the smallest surface particles are dissolved as Fe^{2+} in the spinel matrix whereas the larger ones are oxidized as Fe^{3+} mostly in the form of α-Fe_2O_3. The missing proportion of γ-Fe–C after oxidation corresponds to particles located on the surface of the matrix grains for Mg9Fe1R that were oxidized. This proportion corresponds to that of Fe^{2+} (see tables 6 and 7), which is in agreement with the assumption that the γ-Fe–C particles are among the smallest ones. The evolution of the proportions of Fe^{3+} and α-Fe_2O_3 at 80 K and RT reveals a distribution of sizes of the corresponding hematite particles. However, the Fe^{3+} ions dissolved in the spinel matrix are not homogeneously dispersed, as revealed by the
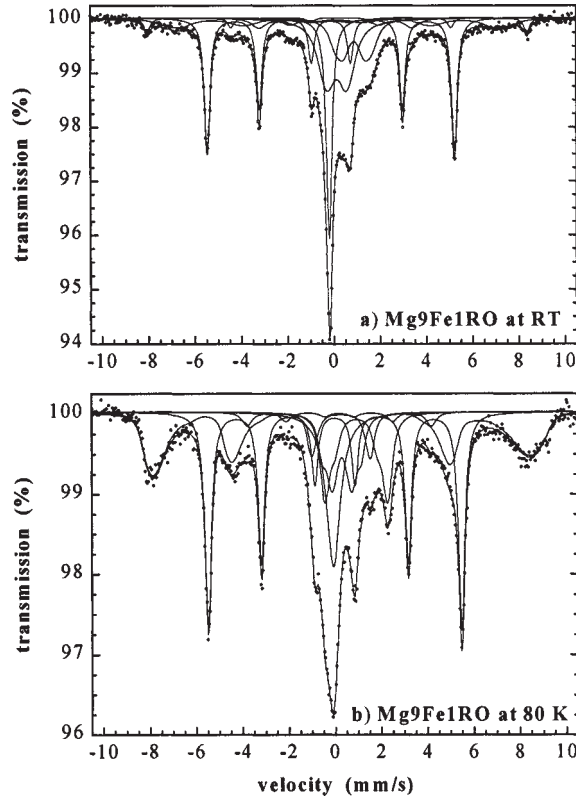
Figure 18. MS spectra of Mg9Fe1RO measured at RT (a) and at 80 K (b).

Table 7
MS parameters of Mg9Fe1RO measured at RT and at 80 K.

	ferro α-Fe					ferro Fe$_3$C					para γ-Fe–C		
	δ	H_{hf}	$2\varepsilon_Q$	Γ	P	δ	H_{hf}	$2\varepsilon_Q$	Γ	P	δ	Γ	P
RT	0.00	332	0.00	0.29	32.5	0.18	205	0.03	0.73	5.5	−0.08	0.29	13.5
80 K	0.11	340	0.00	0.33	33.5	0.31	247	0.00	0.50	3.5	0.04	0.73	13

	α-Fe$_2$O$_3$					ferri MgFe$_2$O$_4$					para Fe^{2+}				para Fe^{3+}			
	δ	H_{hf}	$2\varepsilon_Q$	Γ	P	δ	H_{hf}	$2\varepsilon_Q$	Γ	P	δ	ΔE_Q	Γ	P	δ	ΔE_Q	Γ	P
	0.35	509	−0.17	0.30	3.5	0.26	440	0.00	1.11	11	0.99	1.30	0.55	12.5	0.24	0.90	0.77	21.5
	$\delta = 0.40\ H_{hf} = 510\ 2\varepsilon_Q = 0.05\ \Gamma = 0.36\ P = 27$										1.04	2.30	0.42	12	0.41	0.90	0.41	11

Ferro: ferromagnetic; para: paramagnetic; ferri: ferrimagnetic; H_{hf}: hyperfine field (kOe); δ: isomer shift (mm s^{-1}); ΔE_Q: quadrupole splitting (mm s^{-1}); $2\varepsilon_Q$: quadrupole shift (mm s^{-1}); Γ: line width (mm s^{-1}); P: proportion (%).

presence of a magnetic phase of MgFe$_2$O$_4$. Finally, the very low proportion of Fe$_3$C confirms the hypothesis that this phase is essentially located outside the oxide grains.

4.   Conclusions

The selective reduction in H_2 of $MgAl_2O_4$-based solid solutions produces nanocomposite powders in which transition metal nanoparticles (Fe, Fe/Co, Fe/Ni) are dispersed inside and on the surface of the oxide matrix grains. When using a H_2/CH_4 reducing atmosphere, the metal nanoparticles that form on the surface of the oxide grains act as catalysts for the *in situ* nucleation and growth of single-wall and thin multiwall carbon nanotubes. The oxides and the composite powders (Fe–, Fe/Co– and Fe/Ni–$MgAl_2O_4$, CNTs–Fe/Fe_3C–$MgAl_2O_4$) are characterized using a combination of techniques including ^{57}Fe Mössbauer spectroscopy. Results have been obtained on the crystallographic and magnetic nature of the metal particles, on the composition in the case of alloys and on the localization of the metal or carbide particles on the surface of or inside the spinel grains. It was notably shown that the particles responsible for the formation of the carbon nanotubes appear as Fe_3C in the post-reaction analysis. Future directions of work include a Mössbauer spectroscopy study of CNTs–Fe/M–$MgAl_2O_4$ (M = Co, Ni) powders.

References

[1] R.A. Roy and R. Roy, Mater. Res. Bull. 19 (1984) 169.
[2] R. Roy, S. Komarneni and D.M. Roy, Mater. Res. Soc. Symp. Proc. 32 (1984) 347.
[3] R. Roy, in: *Ceramic Microstructures '86. Role of Interfaces*, eds. J.A. Pask and A.G. Evans, Mater. Sci. Res. 21 (1986) 25.
[4] S. Komarneni, J. Mater. Chem. 2 (1992) 1219.
[5] Ch. Laurent and A. Rousset, Key Eng. Mater. 108–110 (1995) 405.
[6] X. Devaux, Ch. Laurent and A. Rousset, NanoStruct. Mater. 2 (1993) 339.
[7] Ch. Laurent, J.J. Demai, A. Rousset, K.R. Kannan and C.N.R. Rao, J. Mater. Res. 9 (1994) 229.
[8] X. Devaux, Ch. Laurent, M. Brieu and A. Rousset, J. All. Comp. 188 (1992) 179.
[9] Ch. Laurent, A. Rousset, M. Verelst, K.R. Kannan, A.R. Raju and C.N.R. Rao, J. Mater. Chem. 3 (1993) 513.
[10] A. Rousset, J. Solid. State Chem. 111 (1994) 164.
[11] M. Verelst, K.R. Kannan, G.N. Subbanna, C.N.R. Rao, M. Brieu and A. Rousset, Mater. Res. Bull. 28 (1993) 293.
[12] Ch. Laurent, Ch. Blaszczyk, M. Brieu and A. Rousset, NanoStruct. Mater. 6 (1995) 317.
[13] V. Carles, M. Brieu, J.J. Demai and A. Rousset, in: *Fourth Euro-Ceramics*, Vol. 1, ed. C. Galassi (Gruppo Editoriale Faenza Editrice S. p. A., 1995) p. 323.
[14] V. Carles, M. Brieu and A. Rousset, NanoStruct. Mater. 8(5) (1997) 529.
[15] V. Carles, Ch. Laurent, M. Brieu and A. Rousset, J. Mater. Chem. 9 (1999) 1003.

[16] O. Quénard, Ch. Laurent, M. Brieu and A. Rousset, NanoStruct. Mater. 7 (1996) 497.

[17] O. Quénard, E. De Grave, Ch. Laurent and A. Rousset, J. Mater. Chem. 7 (1997) 2457.

[18] A. Marchand, X. Devaux, B. Barbara, P. Mollard, M. Brieu and A. Rousset, J. Mater. Sci. 28 (1993) 2217.

[19] A. Marchand, B. Barbara, P. Mollard, G. Fillion, X. Devaux and A. Rousset, J. Magn. Magn. Mater. 116 (1992) 64.

[20] Ch. Laurent, E. Dooryhée, C. Dufour, F. Gourbilleau, M. Levalois, G. Nouet and E. Paumier, Nucl. Methods Phys. Res. B 107 (1996) 232.

[21] X. Devaux, Ch. Laurent, M. Brieu and A. Rousset, C. R. Acad. Sci. Paris 312 (1991) 1425.

[22] A. Peigney, Ch. Laurent, F. Dobigeon and A. Rousset, J. Mater. Res. 12 (1997) 613.

[23] S. Iijima, Nature 354 (1991) 56.

[24] M.S. Dresselhaus, G. Dresselhaus and P.C. Ekiund, in: *Science of Fullerenes and Carbon Nanotubes* (Academic Press, San Diego, 1995).

[25] C. Journet and P. Bernier, Appl. Phys. A 67 (1998) 1.

[26] Ch. Laurent, E. Flahaut, A. Peigney and A. Rousset, New J. Chem. 22 (1998) 1229.

[27] J.H. Hafher, M.J. Bronikowski, B.K. Azamian, P. Nikolaev, A.G. Rinzler, D.T. Colbert, K.A. Smith and R.E. Smalley, Chem. Phys. Lett. 296 (1998) 195.

[28] E. Flahaut, A. Peigney, Ch. Laurent and A. Rousset, J. Mater. Chem. 10 (2000) 249.

[29] Ch. Laurent, A. Peigney and A. Rousset, J. Mater. Chem. 8 (1998) 1263.

[30] E. Flahaut, A. Govindaraj, A. Peigney, Ch. Laurent, A. Rousset and C.N.R. Rao, Chem. Phys. Lett. 300 (1999) 236.

[31] A. Govindaraj, E. Flahaut, Ch. Laurent, A. Peigney, A. Rousset and C.N.R. Rao, J. Mater. Res. 14 (1999) 2567.

[32] A. Peigney, Ch. Laurent and A. Rousset, J. Mater. Chem. 9 (1999) 1167.

[33] P. Coquay, E. De Grave, R.E. Vandenberghe, C. Dauwe, E. Flahaut, Ch. Laurent, A. Peigney and A. Rousset, Acta Mater. 48 (2000) 3015.

[34] N.M. Rodriguez, J. Mater. Res. 8 (1993) 3233.

[35] H. Dai, A.G. Rinzler, P. Nikolaev, A. Thess, D.T. Colbert and R.E. Smalley, Chem. Phys. Lett. 260 (1996) 471.

[36] A.M. Cassell, J.A. Raymakers, J. Kong and H. Dai, J. Phys. Chem. 103 (1999) 6484.

[37] J.-F. Colomer, G. Bister, I. Willems, Z. Konya, A. Fonseca, G. Van Tendeloo and J.B. Nagy, Chem. Commun. (1999) 1343.

[38] O. Quénard, Doctoral thesis, Toulouse (1997).

[39] J.J. Kingsley and K.C. Patil, Mater. Lett. 6 (1988) 427.

[40] C.E. Johnson, M.S. Ridout and T.E. Cranshaw, Proc. Phys. Soc. 81 (1963) 1079.

[41] M. Hansen, in: *Constitution of Binary Alloys* (McGraw-Hill, New York, 1958) p. 678.

[42] S. Tomiyoshi, H. Yamamoto and H. Watanabe, J. Phys. Soc. Japan 30 (1971) 1605.

[43] H. Rechenberg, L. Billard, A. Chamberod and M. Natta, Phys. Chem. Solids 34 (1973) 1251.

[44] U. Gonser, S. Nasu and W. Kappes, J. Magn. Magn. Mater. 10 (1979) 244.

[45] H. Ullrich and J. Hesse, J. Magn. Magn. Mater. 45 (1984) 315.

[46] I. Ortalli, A. Vera, G. Fratucello and F. Ronconi, Hyp. Interact. 28 (1986) 1025.

[47] R.J. Weiss, Proc. Phys. Soc. 82 (1963) 281.

[48] Y. Nakamura, M. Shiga and N. Shikazono, J. Phys. Soc. Jpn. 19 (1964) 1177.

[49] E.I. Kondorski and V.L. Sedov, J. Appl. Phys. 31 (1960) 331S.

[50] S. Kachi and H. Asano, J. Phys. Soc. Jpn. 27 (1969) 536.

[51] D.G. Rancourt, S. Chehab and G. Lamarche, J. Magn. Magn. Mater. 78 (1989) 129.

[52] J.M. Crowell and J.C. Walker, in: *Proc. 5th Int. Conf. on Mössbauer Spectroscopy*, eds. M. Hucl and T. Zemcik (Czechoslovak Atomic Energy Commission Nuclear Information Center, Prague, 1975) p. 289.

[53] G. Le Caër, J.M. Dubois and J.P. Sénateur, J. Solid State Chem. 19 (1976) 19.